Multi-species ion acceleration from sub-ps, PW interactions with ultra-thin foils

O McCusker[1] ⓘ, H Ahmed[1,2,*] ⓘ, A McIlvenny[1] ⓘ, P Martin[1] ⓘ, S Ferguson[1] ⓘ, J Green[2], J Jarrett[3], M King[3] ⓘ, S Zhai[1,4] ⓘ, P McKenna[3] ⓘ, S Kar[1] ⓘ and M Borghesi[1,*] ⓘ

[1] Centre for Plasma Physics, Queen's University, Belfast BT7 1NN, United Kingdom
[2] Central Laser Facility, STFC Rutherford Appleton, Oxfordshire OX11 0QX, United Kingdom
[3] SUPA Department of Physics, University of Strathclyde, Glasgow G4 0NG, United Kingdom
[4] State Key Laboratory of High Field Laser Physics, Shanghai Institute of Optics and Fine Mechanics, Chinese Academy of Sciences, Shanghai 201800, People's Republic of China

E-mail: hamad.ahmed@stfc.ac.uk and m.borghesi@qub.ac.uk

CrossMark

Abstract

Multi-species ion acceleration from ultra-thin foils was studied experimentally, employing the Vulcan Petawatt laser at the Central Laser Facility, UK. Plastic (CH) foils with thicknesses in the range 10–340 nm were irradiated with intense, short (750 fs) laser pulses producing maximum energies of $\sim$65 MeV and 25 MeV/nucleon obtained for H^+ and C^{6+} ions, respectively. Ion spectra obtained from high resolution spectrometers suggest differences in the acceleration dynamics for the two species. Comparisons are made with two-dimensional Particle in Cell simulations, which identify, for an optimal thickness, two main mechanisms contributing to the ion acceleration process, namely multi-species target normal sheath acceleration (TNSA) and radiation pressure acceleration (RPA). Ion energies are further enhanced by the onset of relativistically induced transparency. A final stage in the acceleration is caused by the formation of electron jets (as the target undergoes transparency), which accelerate the ions off-axis. By analysing the spatial and temporal evolution of the accelerating fields, we are able to infer the effect of the different mechanisms on each species and how this translates to the experimental observations. The two main mechanisms, TNSA and RPA, are seen to each produce a distinct population of high energy protons whereas a single population of carbon is accelerated by a summation of these effects. This species-specific analysis sheds new light on the complex dynamics in a multi-species target expansion and on the contribution of different acceleration processes to the acceleration of the most energetic ions in the spectrum.

Keywords: laser-driven ion acceleration, target normal sheath acceleration,
radiation pressure acceleration, transparency enhanced acceleration

(Some figures may appear in colour only in the online journal)

---

* Authors to whom any correspondence should be addressed.

1. Introduction

Laser driven ion acceleration has gained significant attention in light of many unique properties of the accelerated beams such as high brightness, ultrashort emission and ultra-low beam emittance [1, 2]. These beams offer prospects for developing compact accelerators, with a range of potential applications in healthcare [3], industry and nuclear physics [4, 5]. Despite encouraging developments, improvements must be made in terms of energy conversion efficiency, spectral beam control and energy selection before these ions can be efficiently employed in several of these applications [6].

The most studied and easily attainable acceleration mechanism is target normal sheath acceleration (TNSA) [7, 8], where electrons accelerated by the laser on the front surface of an irradiated foil propagate through the target forming a quasi-electrostatic sheath field on the order of TV m^{-1} at the target rear, where ions are then accelerated. Lighter ions, such as protons, are preferentially accelerated in this scheme due to their higher charge-to-mass ratio. Since standard TNSA generates an exponential energy spectrum and is characterised by a relatively slow ion energy scaling with intensity, generating ion energies and fluxes able to meet the requirements of advanced applications (e.g. in the medical field), remains a significant challenge, particularly for heavier ions, motivating the investigation of advanced acceleration schemes.

Despite requiring much more stringent conditions, radiation pressure acceleration (RPA) [9] is gaining significant research interest. In this scheme, acceleration occurs via the charge separation caused by the laser pressure acting on the target surface and pushing plasma electrons inwards [10]. RPA is typically discussed in two regimes: hole boring (HB) and light sail (LS). HB acceleration occurs when the laser pulse interacts with a target and drives electrons inwards due to the radiation pressure. This pile-up of electrons generates an electrostatic field through the charge separation. An equilibrium is set up where this electrostatic field is balanced by the pondermotive force. Ions left behind will be accelerated by this electrostatic field. Once they reach the edge of the skin layer the equilibrium collapses and fastest ions will break away at a velocity that is twice the velocity of the HB front, $\sim 2v_{HB}$. If the laser pulse has not ended at this stage the process will repeat and therefore HB acceleration can be described as cyclic [10–12].

If the target is thin enough that the HB front reaches the target rear ($l < v_{HB}\tau_L$, where v_{HB} is the HB velocity and τ_L is the laser pulse duration) [10, 13–15] the compressed target layer can then enter the LS phase where the ions are coherently accelerated as one moving mass [16]. RPA provides a far superior ion energy scaling with intensity (HB: $E_{max} \propto I$ and LS: $E_{max} \propto I^2$) compared to conventional TNSA ($E_{max} \propto I^{0.5}$) and has the potential to produce narrow-band ion beams. However it is difficult to obtain as RPA requires the target to remain opaque to the laser pulse and so ceases with the onset of relativistically induced transparency (RIT). RIT occurs if $a_0 > \omega_p^2 l / 2c\omega_L$, where a_0 is the dimensionless laser strength parameter, c is the speed of light in a vacuum, ω_p is the classical plasma frequency (i.e. without relativistic corrections)

and ω_L is the laser frequency. It is caused by a combination of plasma expansion and a relativistic increase in electron inertia and leads to $\omega_p/\gamma^{0.5} < \omega_L$, meaning there is no longer a critical surface (CS) to reflect incident light and the remainder of the pulse propagates through the expanded target [17].

Acceleration in relativistically transparent plasmas has been discussed in terms of the so-called BreakOut After-Burner regime, which allows direct heating of the 'cold' ions which have remained within the target bulk [18]. Under suitable conditions, target transparency has been seen to enhance the magnitude of the electrostatic accelerating fields as a result of enhanced volumetric heating of the bulk plasma electrons [19]. For example, in [20] it was shown that this mechanism was dominant for the acceleration of carbon ions, for target thicknesses such that the target became relativistically transparent close to the arrival of the peak of the pulse. Transparency enhanced TNSA [21] and more recently enhanced hybrid TNSA-RPA acceleration [22], in a scenario similar to the one discussed here have been reported. The focus of these recent studies has mostly been on the acceleration of protons, with impressive results leading to proton energies near the 100 MeV threshold [22]. The results reported here differ from those discussed in [22], as they include Thomson parabola spectrometer (TPS) data which allows characterizing different ion species within the beam, and helps to further elucidate the multi-species dynamics taking place during the acceleration process. Whilst [22] credits a hybrid TNSA-RPA scheme enhanced by transparency for the acceleration of the highest energy protons, this does not appear to be the case here. While the same mechanisms are identified it is found that, in accelerating the highest energy protons, the mechanisms act independently of each other, i.e. not in a *hybrid* fashion. On the contrary, for what concerns the acceleration of C^{6+} ions, a summation of these mechanisms produces the highest energies. In this context, relevant particle in cell (PIC) simulations are a very important tool in identifying the contribution of these different mechanisms and to pinpoint where within the target the highest energy ions originate from. Through the comparison of experimental and PIC simulation results, this paper aims to clarify the interplay and contribution of different acceleration processes for the two main species accelerated (protons and C^{6+} ions), an aspect which has not been analysed in detail in previous studies and is of general relevance for the optimization of the interaction with, and acceleration from, ultrathin foils.

2. Experimental set-up and results

The experimental campaign was carried out using the petawatt arm of the Vulcan laser at the Central Laser Facility, UK. The laser was linearly polarised, and focused using an f/3 off-axis parabolic mirror to a Gaussian spot of 5 μm (FWHM). A plasma mirror was also used for temporal contrast enhancement. The pulse duration was typically around 750 fs (FWHM) containing a total energy of $\sim$210 J with $\sim$35% of this in the FWHM of the focal spot, leading to peak intensities within the range (3–5)$\times 10^{20}$ W cm^2 (these parameters varied from
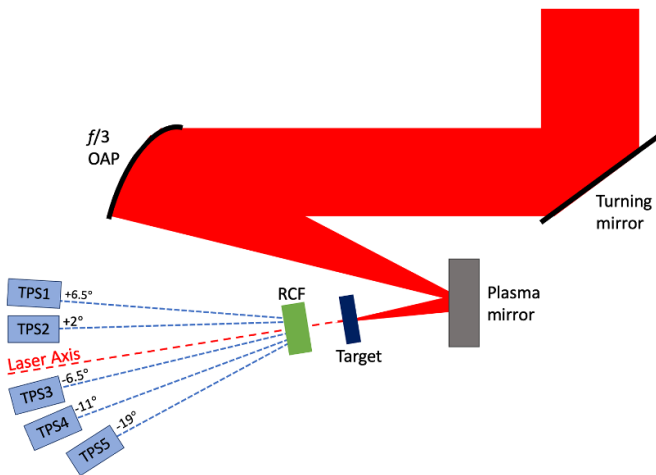
Figure 1. A schematic of the experimental setup showing laser pulse (red) focused using an *f*/3 parabola onto the target at normal incidence.
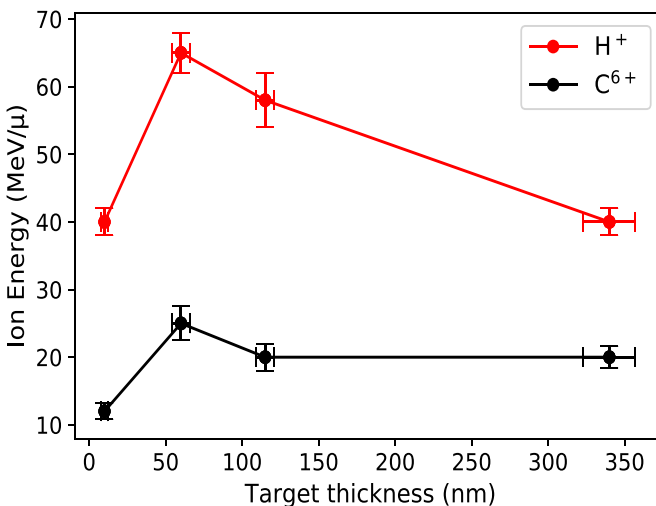

Figure 2. Maximum energies obtained experimentally from TPS1 for both H^+ (red) and C^{6+} (black) ions. Vertical error bars come from the resolution of the TPS and the horizontal error bars from the uncertainty in the measurement of the target thicknesses.

shot to shot). Plastic (CH) targets of various thicknesses in the range 10–340 nm were used and aligned so that the surface was normal to the laser axis. The main diagnostics were TPSs, placed in the forward direction at five different angles: 6.5°, 2°, −6.5°, −11° and −19° with respect to the laser axis and a radiochromic film (RCF) stack placed behind the targets rear surface. The RCF stacks only captured the upper half of the beam, allowing ions to reach the TPS placed behind. The TPS were used in conjunction with BAS-TR image plate detectors, whose responses have been calibrated with respect to different ion species [23, 24]. A schematic of the experimental set-up can be seen in figure 1.

An optimal target thickness, in the range studied, for acceleration of both H^+ and C^{6+} ion species was obtained from a target thickness scan, shown in figure 2. Maximum energy for both species is observed at 60 nm, i.e. ~65 MeV for protons and 25 MeV/u for carbon ions. Due to the limited amount of target thicknesses available at the time of the experiment, we were unable to pinpoint more precisely the optimal thickness value, which, if we also consider the information in [22], may lie between 60 and 100 nm. An overall similar trend in the maximum energies achieved as a function of target thickness is seen for the two species.

Maximum energies were obtained on TPS1 placed at +6.5°; a comparison of the spectra obtained for different target thicknesses at this angle is shown in figure 3.

As can be seen, all spectra are quite modulated and have profiles, which differ significantly from a typical exponential TNSA spectrum. A peak in the flux is seen for low energy protons (10–20 MeV) for the 10 and 340 nm target. A similar feature is also seen for the remaining targets (60 and 115 nm) however it is significantly broader and extends at higher energies, beginning at ∼20 MeV for both targets. For the carbon ion spectra, some similarities are also seen between 10 and 340 nm, as well as between the 60 and 115 nm targets. The ion flux decays with increasing ion energy for 10 and 340 nm targets, while for the other two targets a spectral peak is observed at the highest energies (around 10–25 MeV/u) towards the end of the spectra. The thinnest target (10 nm) records the lowest energies for both species, suggesting a significant decrease in the efficiency of the acceleration or quality of the interaction. In comparison, the thickest target (340 nm), records similar proton energies to the 10 nm target, but double the carbon ion energy. This suggests differences in the acceleration processes between the two species and for the various target thicknesses, which are further investigated in section 3.

For the optimal thickness of 60 nm, information on the angular distribution for both species is reported in figure 4, showing the spectra obtained along the different observation lines. Although the highest proton energies (∼65 MeV) are detected along TPS1—significant energies are also detected on the other Thomson parabolas and even at the larger angle of −19°, albeit with a lower flux in comparison to the TPS's placed between −6.5° and +6.5°. Carbon ion energies are similar across all angles (20–25 MeV/u) indicating a larger beam divergence in contrast with the proton beam, which displays a clear directional preference for the high energy component (TPS1 at +6.5°).

The off-axis acceleration of the proton beam is further confirmed from the spatial profile obtained from the RCF. Figure 5 shows selected RCF layers for the optimal target thickness of 60 nm. At lower energies (layers labelled 12 and 17 MeV) the ion beam is centred around the laser axis. However, in the higher energy RCF layers, a shift in the beam to the side is seen. The direction of the beam also agrees with the TPS results, as highest energies are detected at +6.5°, with respect to the laser axis, the same direction to which the beam is pointing in the highest energy RCF layers. As the carbon ions will stop in earlier layers of the RCF their spatial profile cannot be isolated from the RCF data, as the dose deposited in these layers comes from both species [25].
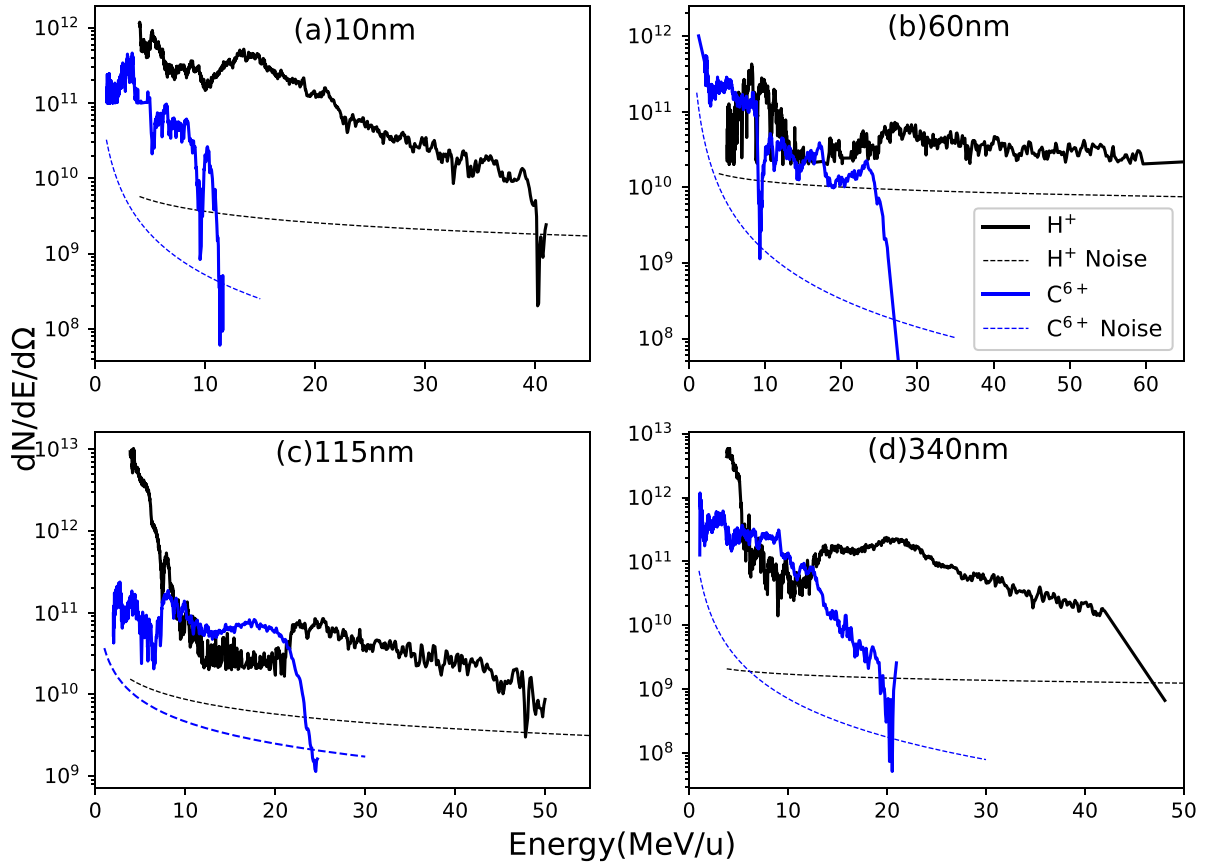
Figure 3. Spectra obtained for both H^+, (a), and C^{6+}, (b), ions at TPS1 ($+6.5°$) for each target thickness, 10, 60, 115 and 340 nm. Dashed lines represent background noise level.
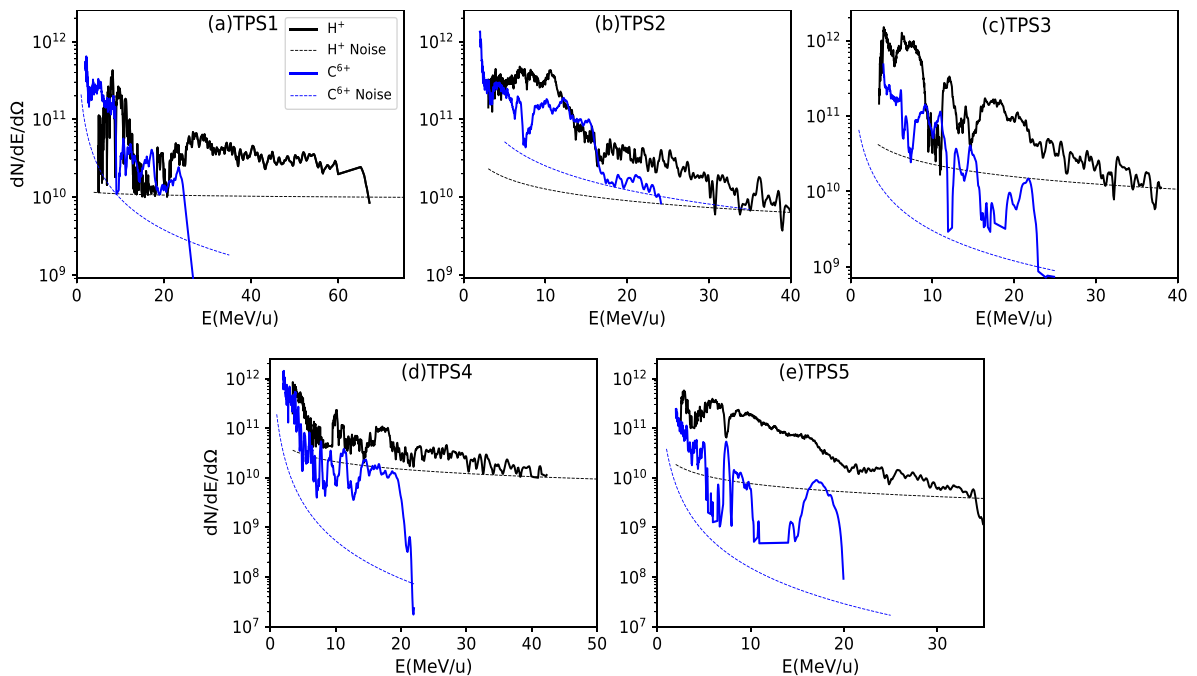

Figure 4. Spectra obtained for both H^+ (black) and C^{6+}(blue) ions at each TPS for optimal thickness 60 nm. TPS1 $= +6.5°$, TPS2 $= +2°$, TPS3 $= -6.5°$, TPS4 $= -11°$ and TPS5 $= -19°$, with respect to the laser axis.

For the other target thicknesses investigated, a preferential direction for the acceleration of the protons is also seen, although the direction is random and therefore not consistent between the shots. Acceleration of C^{6+} ions is less directional, with similar energies being obtained across multiple TPS for each target thickness.
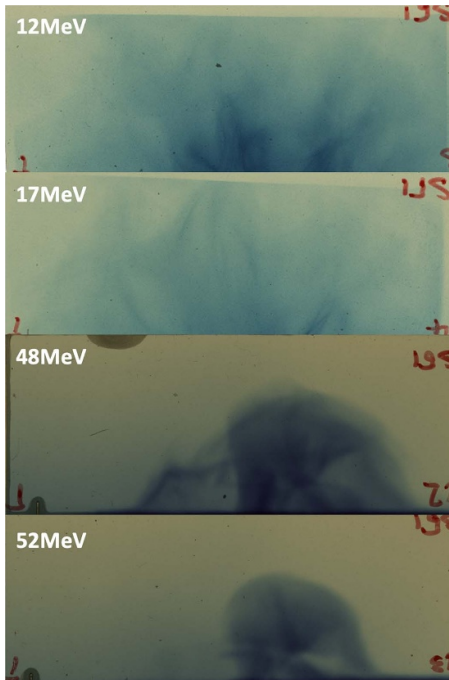
Figure 5. Layers at various energies from an RCF stack showing the ion beam profiles from the optimal thickness, 60 nm CH, shot. Proton Bragg peak energies for each layer are labelled in the top left corner. The C^{6+} ions will only reach the first RCF layer shown (with proton Bragg peak energy 12 MeV). Therefore the later RCF layers shown represent proton only beam profiles. The layers with Bragg peak energies 12 and 17 MeV are HDV2 and the layers labelled 48 and 52 MeV are EBT3.

In order to explain the origin of the differences in spectral profile and angular distribution observed for the two ion species, we have explored the acceleration dynamics through a programme of 2D PIC simulations.

3. 2D pic simulations

The relativistic PIC code EPOCH [26] was used to carry out 2D simulations. The targets were initialised with an electron density of $600n_c$, where n_c is the critical density, for the laser pulse of wavelength 1054 nm, ($\sim 1 \times 10^{21}$ cm^{-3}) and neutralised with either a uniform mixture of both C^{6+} and H^+ ions (to simulate the CH targets used in the experiment) or H^+ ions (for the single species hydrogen targets, introduced as comparators to identify and isolate any multi-species effects in CH). The size of the simulation box was $80\,\mu m \times 20\,\mu m$ in **x** and **y**, with a mesh cell size equal to $5\,nm \times 10\,nm$, respectively. Each ion species had 250 particles per cell loaded into the simulation. To account for any uncertainty in the experimental measurements, various sets of simulations were ran to investigate a range of laser parameters. The temporal profile of the laser pulse was Gaussian, with intensity profiles having FWHM duration equal to either 400, 500 and 600 fs. The use of shorter pulse lengths in these simulations compared to the experiment is motivated by the exaggerated target heating and expansion associated to the 2D geometry. A comparison of 2D and 3D simulations has been carried out in [27]

which shows increased electron heating for 2D simulations. Therefore, using a shorter pulse length will ensure that the laser pulse interacts with a more realistic target density profile, more in line with what we would expect in 3D. The spatial intensity profile in the focal spot was also Gaussian, with a FWHM of $5\,\mu m$. Peak intensities were within the range (3–5) $\times 10^{20}$ W cm^{-2}. The laser energy was kept constant as this was in line with what was achieved experimentally, where the largest uncertainty in the laser parameters was the pulse length, which has been varied in our simulations to reflect this (between 400 and 600 fs). Due to the use of a plasma mirror in the experimental set-up, pre-plasma formation is considerably suppressed and therefore not considered in the simulations.

Initially a thickness scan was carried out, for different pulse lengths, showing that the optimal target thicknesses remains consistently in the range 100–140 nm, as seen in figure 6. Similar to the experimental situation, there is some uncertainty in these values due to the finite number of thicknesses investigated. To further pinpoint an optimal target thickness, for a set of simulations with pulse length 400 fs, two extra thicknesses were included (120 and 170 nm). This indicates 140 nm as the optimal thickness amongst those investigated. The thicknesses at which the proton energy reaches its maximum are larger for the simulations than observed in experiments, similar to the work discussed in [27]. The reduced dimensionality of the simulations will cause an earlier onset of transparency at a given thickness and therefore the requirement of a thicker target for optimal acceleration. The enhanced heating also typically results in an overestimation of the ion energies, as also observed here.

Analysis of all sets of input parameters reveal a similar acceleration process for the optimal thickness of each set of simulations. This suggests that the acceleration scenario presented is robust regardless of the exact values of the laser parameters. The set of simulations which displayed the most efficient acceleration and ion energies (pulse duration FWHM equal to 0.4 ps and intensity $\sim 5 \times 10^{20}$ W cm^{-2}) will be discussed in detail in the following. Consistently with what has been reported in [22], highest ion energies are obtained when the target is seen to undergo transition to transparency close to the peak of the irradiating pulse.

The acceleration dynamics and the effects of target transparency were initially studied. For an optimal target thickness (140 nm), the evolution of the electric (accelerating) field and the resulting ion densities were compared for the CH target and pure proton target with the same electron density to investigate the effects of the presence of multiple ion species while ensuring physical processes such as HB are directly comparable between the cases; these are shown for three time steps in figure 7.

Figure 7(a) highlights the sheath electric field formed at the target's rear surface. Expansion of the ion densities at this point differs between the multi-species target (top row) and the pure proton target (bottom row). In CH, a distinct forward peak in the proton density (indicated by the green arrow in figure 7(a)), is closely followed by a carbon front. In comparison, an exponential proton density profile is seen for a pure proton target throughout the interaction (figures 7(d)–(f)). The forward peak
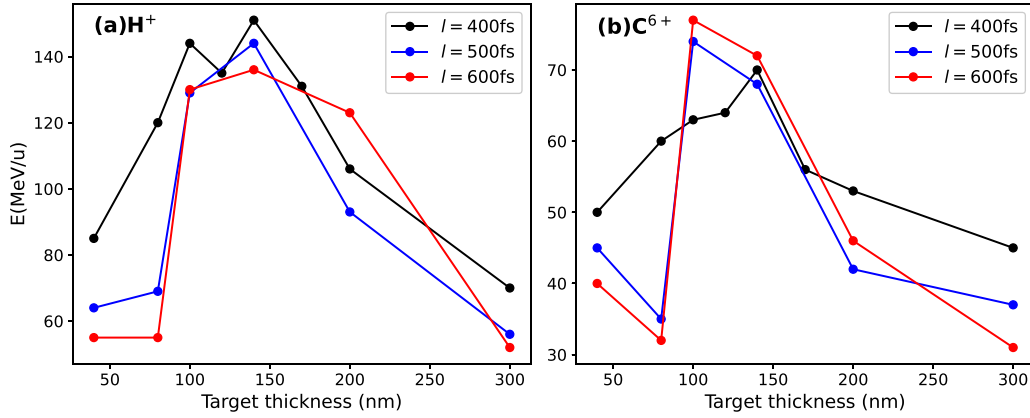
Figure 6. Maximum energies obtained from PIC simulations for both H^+ (a) and C^{6+} (b) ions. Pulse length and peak intensity were varied, however the total laser energy remained constant.
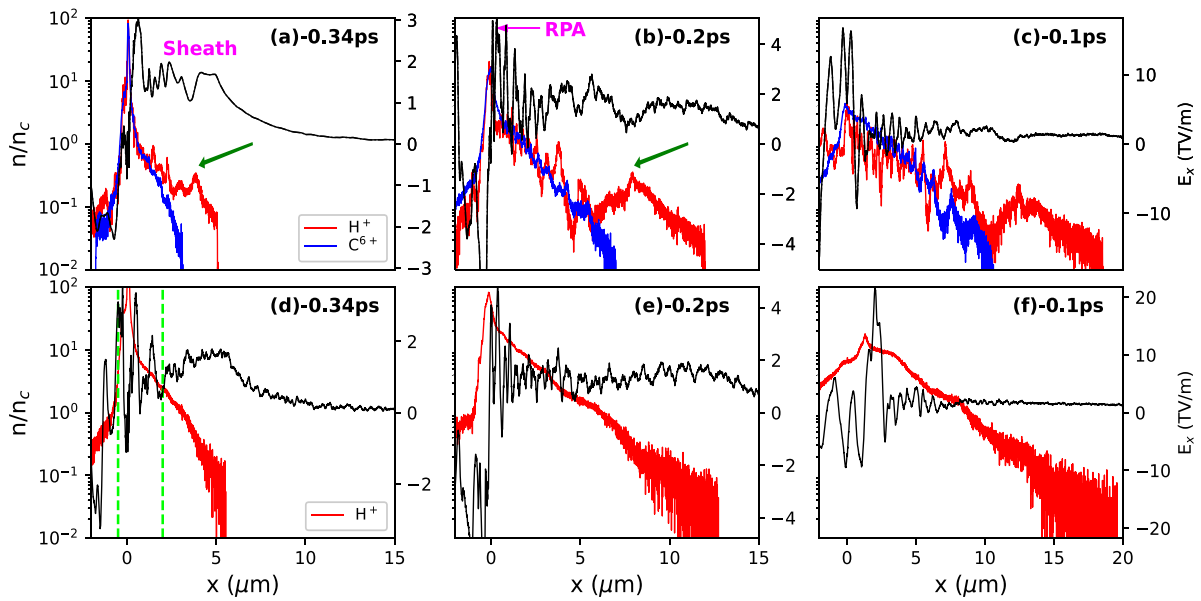

Figure 7. Cycle averaged electric fields (along the laser axis) E_x (black), with H^+ (red) and C^{6+} (blue) density for CH target (top row). The equivalent pure proton target is compared (bottom row) for the same times. (a) and (d) are taken at $t = -0.34$ ps, (b) and (e) are taken at $t = -0.2$ s and (c) and (f) $= -0.1$ ps, where $t = 0$ ps corresponds to the peak of the pulse arriving at the targets initial front surface position, located at $x = 0\,\mu$m. Green arrows in (a) and (b) indicate the most forward energetic peak in the proton density, influenced by both the TNSA field the presence of C^{6+} within the target. The dashed green lines in (d) highlight the region where the modulations in the field (discussed in text) are located.

in the proton density for CH targets is still obvious at later times (arrow in figure 7(b)), with the carbon front following closely behind. This suggests the sheath expansion of the protons is influenced by the presence of the carbon ions within the target. Modulations in the E_x field are seen for both targets, but they form earlier in the hydrogen only target, as seen in the region enclosed by the dashed green lines in figure 7(d). The simulations suggest that these trailing modulations arise when the bulk plasma expands into the rarefied rear plasma generated by the TNSA field.

Numerous proton peaks can be seen forming later in the interaction, closer to the CH target bulk. Since no such peaks ever form in the pure proton target, it is likely that these peaks may arise due to the presence of carbon within the target and local modulations in the carbon density. The situation may be

similar to the two species expansion investigated in [28] discussing how the lighter species is accelerated ahead of a heavy ion front and the effects this has on each species' density.

Despite multi-species TNSA playing a main role in the initial acceleration, it is not responsible for the maximum field strength seen at around $x = 0\,\mu$m, prior to transparency and the arrival of the peak of the pulse. To investigate this point further the changes in ion densities are plotted around this time in figure 8.

While the target has already pre-expanded prior to the peak of the pulse arriving, the increasing laser intensity will act on the remaining (overdense) target bulk. Figure 8 highlights the effect this has on the remaining bulk ions. Remaining bulk protons are pushed forward, moving with the CS and behind a peak in the electron density (as shown in figure 8), which is
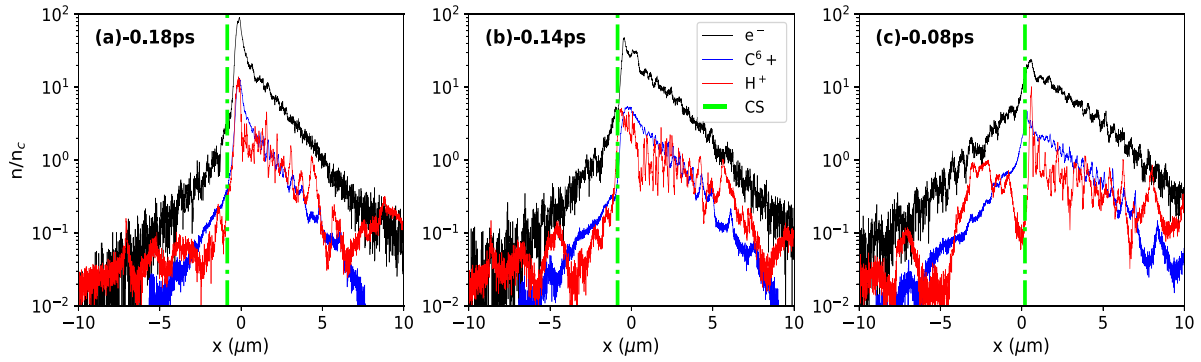
Figure 8. Expansion of ion (proton, carbon and electrons) densities prior to the peak of the pulse arriving and the target undergoing transparency. The green dashed line represents the CS.
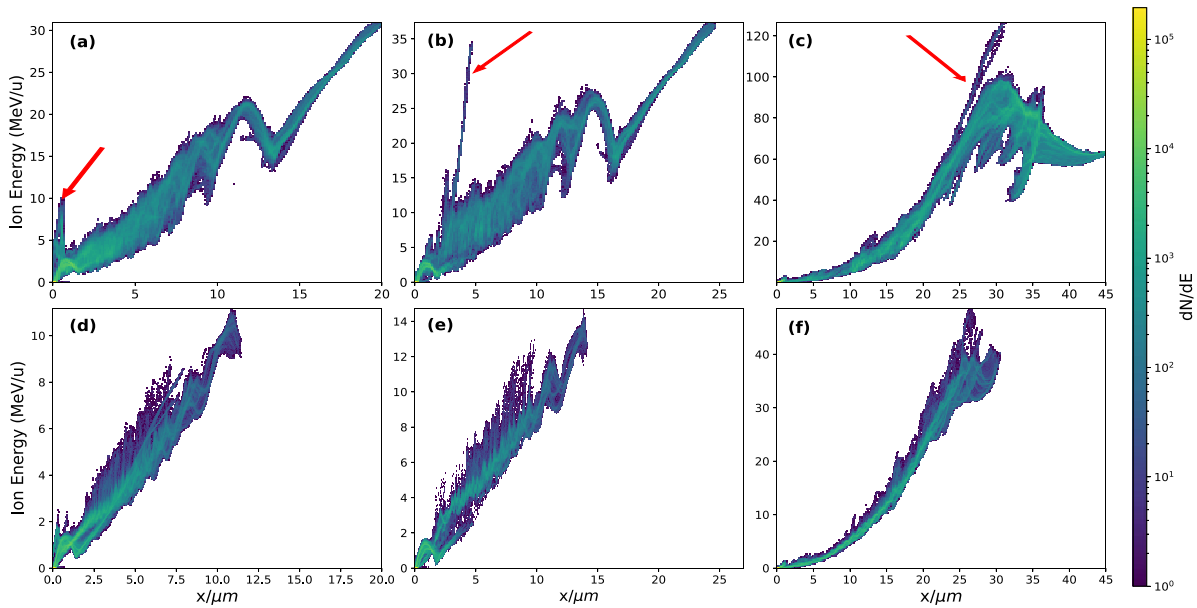

Figure 9. Phase space for both ion species; protons (top row) and C^{6+} ions (bottom row) for three different time steps; $t = -0.08$ ps (a) and (d), $t = -0.02$ ps (b) and (e), and $t = 0.22$ ps (c) and (f), where $t = 0$ ps corresponds to the peak of the pulse arriving at the targets initial front surface position. Labelled with a red arrow in (a)–(c) are the RPA protons.

typical of RPA. This pile-up of electrons produces a maximum field strength of ~ 12 TV m^{-1}. At this point, spatial separation of the two species is seen within the target bulk which favours the acceleration of protons as they will both shield the carbon ions from the forward accelerating fields and also benefit from the space charge field generated by the carbon ion themselves. At earlier times, RPA would have not yet made a significant contribution, due to the near-solid density of the bulk.

To further confirm the mechanisms which were identified in the simulations and to better show the features in the experimental spectra shown in figure 4, phase space plots for each species are presented in figure 9 for three-time steps. The first-time step was chosen at a time at which the target is undergoing transparency but prior to the peak of the pulse arriving. The RPA bunch of protons is labelled with a red arrow in the proton phase space plots. Through the phase spaces in figures 9(a)–(c), we can confirm that these RPA protons only start their acceleration just before target transparency and will eventually catch up with the initially accelerated high energy TNSA

protons, as seen in figure 9(c)—showing that the two bunches of highest energy protons are initially accelerated independently of each other by two different mechanisms and originate from different parts of the target.

No real distinct features can be identified in the carbon phase space seen in figures 9(d)–(f), similar to the spectra obtained experimentally. The acceleration of carbon ions is harder to characterise with only one bunch reaching maximum energy through a summation of TNSA, RPA and transparency effects. This is likely due to the fact that the carbon ions have a lower charge to mass ratio and will lag behind the initially accelerated protons, which shield them from the maximum effects of the fields and, as a result, no distinct bunches can be identified from the phase space plots.

As in the experiment, the highest energy ions are detected off-axis also in the simulations. Figure 10 shows the angular distribution of the accelerated ions, at the time at which maximum energies are obtained. Both ion species are detected within a cone of $\pm 20°$ aperture. However the highest energy
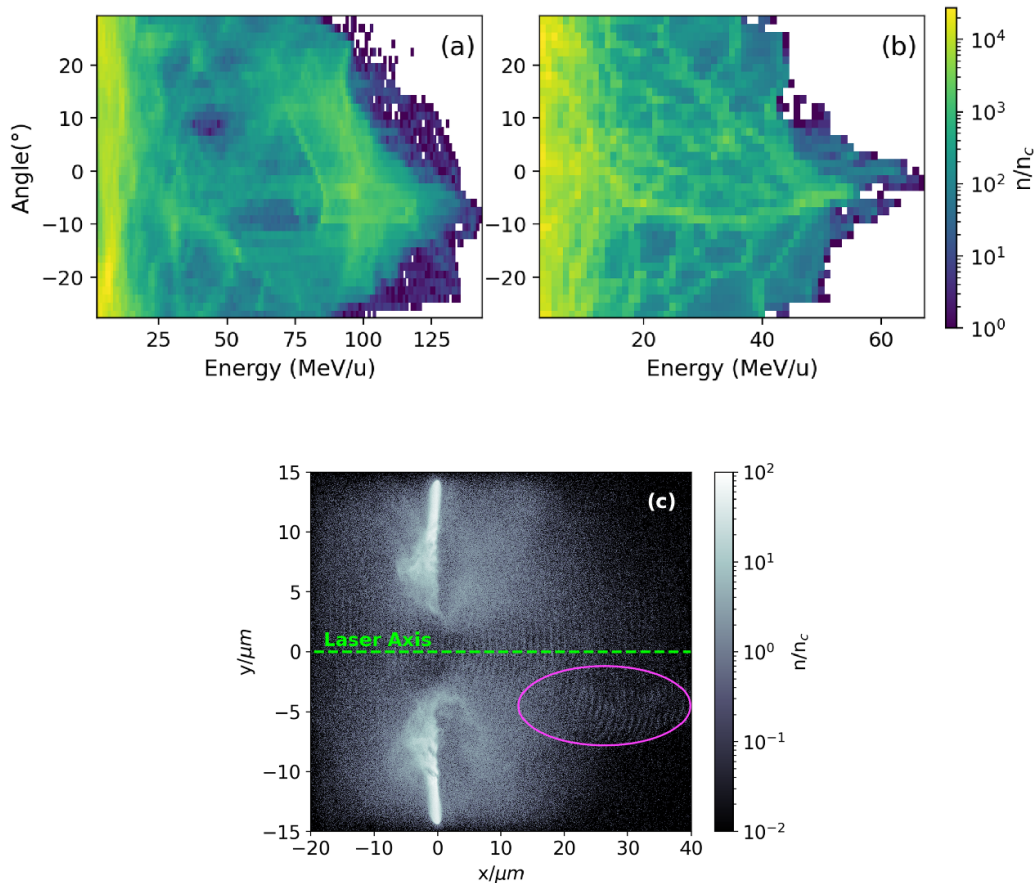
Figure 10. Angular distribution of (a) protons and (b) carbon ions, with corresponding electron density (c), at $t = 0.34$ ps, where $t = 0$ ps is the arrival of the peak of the pulse. The pink circle highlights a hot electron jet formed during the transparency phase, directed off-axis.

ions are preferentially accelerated in a single off-axis direction, as also seen experimentally from the TPS spectra in figure 4.

This ion deflection is likely due to the fields associated with the formation of a hot electron jet during the relativistic transparency phase of the interaction, as discussed in detail in [22, 29, 30]. These jets are quite unstable and despite forming in both directions, with respect to the laser axis, they tend to become more pronounced in one off-axis direction. The random nature of these jets has previously been reported in [22, 29, 30], where their influence on proton acceleration is also discussed. In the work presented here, the jets form a final stage in the acceleration of the ions, as highlighted in figure 10, where it is seen the highest energy protons are emitted at an angle of $\sim 10°$, where an electron jet is also observed (see figure 10(c)). On the contrary, the highest energy carbon ions are emitted at angles $\sim 0°$. This difference may be explained as due to the protons' higher charge to mass ratio, which makes protons more susceptible to the effects of this directional electron jet than the carbon ions. Again, this broadly agrees with the carbon's experimental spectra which did not display any clear off-axis preferential directionality.

Thanks to the simulations, three clear ion acceleration processes have been identified; multi-species TNSA (i.e. TNSA influenced by the presence of different species within the target), which accounts for initial acceleration of rear surface ions; RPA acting on the remaining target bulk and finally the effect of electron jets which form off-axis at later times, which enhance the energies of the protons and propel them off-axis, as reported in [30]. All of these mechanisms will contribute, to a different extent, to the ion spectra observed in the simulations and experimentally. A pertinent question is whether any of these mechanisms is dominant in determining the acceleration of the highest energy ions in the spectra. To determine this, ions within the top 5 MeV/u in the spectra for both species were tracked throughout the interaction. It was found that, for protons, two distinct bunches reached maximum energy; one originating from the target rear surface and one originating from the target bulk. These bunches, although initially spatially separated, combine together to form one bunch of high energy particles by the end of the interaction. Through particle tracking these mechanisms were found to act independently of each other. Only one bunch of carbon ions reached maximum energy and these consistently moved in the sheath field from the beginning of the interaction. These differences can account for the different spectral features recorded experimentally. To summarise the differences in the acceleration, the accelerating field which these high energy ions experience throughout the interaction is plotted over time in figure 11, with the protons split up into their two bunches.

While surface protons experience an accelerating field at the start of the interaction, and are then accelerated by a sheath
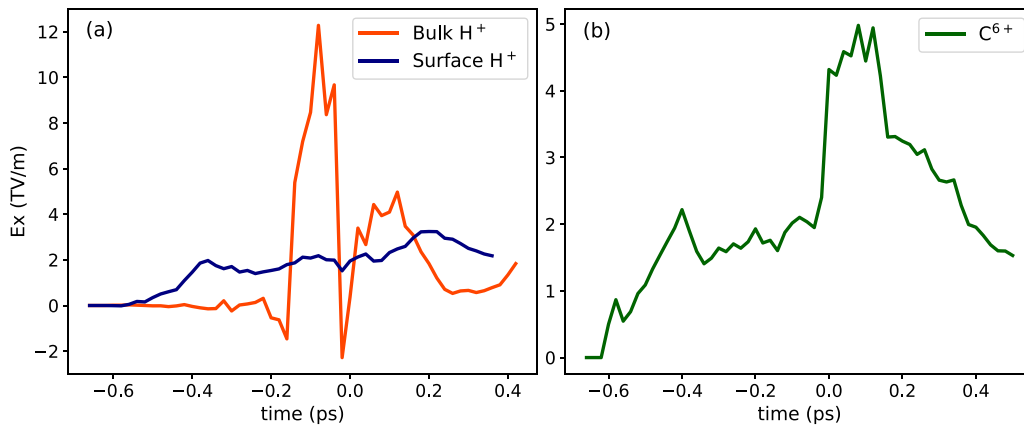
Figure 11. Cycle averaged E_x field experienced by high energy ions (top 5 MeV/u) for; (a) protons and (b) carbon ions.

field of 2–3 TV m^{-1} throughout the interaction, the bulk protons remain stationary within the target until they experience a field of 12 TV m^{-1}, which is around four times the maximum field experienced by the sheath-accelerated protons. Hence, the surface protons are accelerated by a weaker field over a longer period of time (the entire interaction) whilst the bulk protons only begin their acceleration when the RPA field forms (at around -0.2 ps), experiencing a more intense acceleration phase. A dip in the field experienced by the bulk protons is seen around 0 ps, as the target undergoes transparency, before a sharp increase to ~4 TV m^{-1}. As the target is no longer opaque at $t = 0$, the dip in field experienced by the bulk protons at this time is due to the halting of RPA.

The carbon ions, like the surface protons, are accelerated throughout the entire interaction. However, a difference, is that these ions seem to benefit more from the field enhancement as the target undergoes transparency, as seen by a sharp increase in field magnitude (~5 TV m^{-1} in figure 11(b)). Transparency affects both the bulk protons and sheath carbon ions at the same time (0 ps), since they are at the same point in space when transparency occurs. The effect on the surface protons is both delayed and weaker, with only a slight increase in the field seen around 0.2 ps, due to their position further away from the target bulk. Carbon ions within the target bulk do not appear to be affected significantly, unlike the protons, by the RPA field— this may be because the RPA protons will outrun the carbon ions and shield them from the effects of this field. Therefore, carbon ions, which are initially accelerated by the RPA field do not reach significant energies through this progress because of this shielding, similarly to what has been discussed in [31, 32].

4. Conclusions

In conclusion, observations of thickness-dependent proton and carbon ion spectra from ultra-thin foils are interpreted with the help of 2D PIC simulations. PIC simulations corroborate experimental results and elucidate a complex interplay of different mechanisms with differing effect on light and heavy ion species. For instance, high energy protons are observed to originate from both the rear surface and bulk of the target, with rear surface protons having a longer acceleration time. On the

other hand, highest energy carbon ions, similar to rear surface protons, appear to originate from one rear surface bunch and are accelerated throughout the interaction over a longer period of time. A final acceleration boost is given to the protons by the formation of electron jets later in the interaction, which also influences the final direction of the proton beams. These jets have little influence on the highest energy carbon ions, which are detected close to the laser axis. For the highest energy protons (top 5 MeV in the spectrum) these schemes are shown to act independently of each other (i.e., not in a hybrid fashion, as discussed in [22]) on different groups of protons. Whilst the presence of carbon ions within the target bulk benefits the acceleration of protons (by piling forward protons into a peak, enhancing the accelerating field they experience), the fact that protons lead the acceleration, causes the lagging carbon ions (bulk ions) to get shielded from the maximum field strength. These results help to further explain the complex dynamics within a multi-species target expansion. Particle tracking within the PIC simulations proves to be a useful tool for pinpointing which mechanisms produce highest energy ions, which in this case differ between the two species.

Data availability statement

The data that support the findings of this study are openly available at the following URL/DOI: https://doi.org/10.17034/2dd04796-49f2-4960-b433-6b3bc2c70997.

ORCID iDs

O McCusker https://orcid.org/0000-0003-1189-4292
H Ahmed https://orcid.org/0000-0002-2151-8971
A McIlvenny https://orcid.org/0000-0002-1044-1534
P Martin https://orcid.org/0000-0002-0928-7445
S Ferguson https://orcid.org/0000-0003-2646-8018
M King https://orcid.org/0000-0003-3370-6141
S Zhai https://orcid.org/0000-0002-6795-3274
P McKenna https://orcid.org/0000-0001-8061-7091
S Kar https://orcid.org/0000-0002-9406-3103
M Borghesi https://orcid.org/0000-0001-9165-0073

References

[1] Macchi A, Borghesi M and Passoni M 2013 Ion acceleration by superintense laser-plasma interaction *Rev. Mod. Phys.* **85** 751–93

[2] Daido H, Nishiuchi M and Pirozhkov A S 2012 Review of laser-driven ion sources and their applications *Rep. Prog. Phys.* **75** 056401

[3] Bulanov S V, Esirkepov T Z, Khoroshkov V S, Kuznetsov A V and Pegoraro F 2002 Oncological hadrontherapy with laser ion accelerators *Phys. Lett. A* **299** 240–7

[4] Ledingham K W D, McKenna P and Singhal R P 2003 Applications for nuclear phenomena generated by ultra-intense lasers *Science* **300** 1107–11

[5] McKenna P *et al* 2003 Demonstration of fusion-evaporation and direct-interaction nuclear reactions using high-intensity laser-plasma-accelerated ion beams *Phys. Rev. Lett.* **91** 075006

[6] Badziak J 2018 Laser-driven ion acceleration: methods, challenges and prospects *J. Phys.: Conf. Ser.* **959** 012001

[7] Snavely R A *et al* 2000 Intense high-energy proton beams from petawatt-laser irradiation of solids *Phys. Rev. Lett.* **85** 2945–8

[8] Passoni M, Bertagna L and Zani A 2010 Target normal energy sheath acceleration: theory, comparison with experiments and future perspectives *New J. Phys.* **12** 045012

[9] Esirkepov T, Borghesi M, Bulanov S V, Mourou G and Tajima T 2004 Highly efficient relativistic-ion generation in the laser-piston regime *Phys. Rev. Lett.* **92** 175003

[10] Macchi A, Cattani F, Liseykina T V and Cornolti F 2005 Laser acceleration of ion bunches at the front surface of overdense plasmas *Phys. Rev. Lett.* **94** 165003

[11] Robinson A P L, Gibbon P, Zepf M, Kar S, Evans R G and Bellei C 2009 Relativistically correct hole-boring and ion acceleration by circularly polarized laser pulses *Plasma Phys. Control. Fusion* **51** 024004

[12] Robinson A P L, Kwon D-H and Lancaster K 2009 Hole-boring radiation pressure acceleration with two ion species *Plasma Phys. Control. Fusion* **51** 095006

[13] Robinson A P L, Zepf M, Kar S, Evans R G and Bellei C 2008 Radiation pressure acceleration of thin foils with circularly polarized laser pulses *New J. Phys.* **10** 013021

[14] Yu T-P, Pukhov A, Shvets G and Chen M 2010 Stable laser-driven proton beam acceleration from a two-ion-species ultrathin foil *Phys. Rev. Lett.* **105** 065002

[15] Kar S *et al* 2012 Ion acceleration in multispecies targets driven by intense laser radiation pressure *Phys. Rev. Lett.* **109** 185006

[16] Macchi A, Veghini S and Pegoraro F 2009 "Light sail" acceleration reexamined *Phys. Rev. Lett.* **103** 085003

[17] Vshivkov V, Naumova N, Pegoraro F and Bulanov S 1998 Nonlinear electrodynamics of the interaction of ultra-intense laser pulses with a thin foil *Phys. Plasmas* **5** 2727–41

[18] Yin L, Albright B J, Bowers K J, Jung D, Fernández J C and Hegelich B M 2011 Three-dimensional dynamics of breakout afterburner ion acceleration using high-contrast short-pulse laser and nanoscale targets *Phys. Rev. Lett.* **107** 045003

[19] Henig A *et al* 2009 Enhanced laser-driven ion acceleration in the relativistic transparency regime *Phys. Rev. Lett.* **103** 045002

[20] Jung D *et al* 2013 Efficient carbon ion beam generation from laser-driven volume acceleration *New J. Phys.* **15** 023007

[21] Poole P *et al* 2018 Laser-driven ion acceleration via target normal sheath acceleration in the relativistic transparency regime *New J. Phys.* **20** 013019

[22] Higginson A *et al* 2018 Near-100 mev protons via a laser-driven transparency-enhanced hybrid acceleration scheme *Nat. Commun.* **9** 724

[23] Mančić A, Fuchs J, Antici P, Gaillard S and Audebert P 2008 Absolute calibration of photostimulable image plate detectors used as (0.5–20 mev) high-energy proton detectors *Rev. Sci. Instrum.* **79** 073301

[24] Doria D *et al* 2015 Calibration of BAS-TR image plate response to high energy (3–300 mev) carbon ions *Rev. Sci. Instrum.* **86** 123302

[25] Scullion C *et al* 2016 Angularly resolved characterization of ion beams from laser-ultrathin foil interactions *J. Instrum.* **11** C09020

[26] Arber T *et al* 2015 Contemporary particle-in-cell approach to laser-plasma modelling *Plasma Phys. Control. Fusion* **57** 113001

[27] Stark D J, Yin L, Albright B J and Guo F 2017 Effects of dimensionality on kinetic simulations of laser-ion acceleration in the transparency regime *Phys. Plasmas* **24** 053103

[28] Tikhonchuk V T, Andreev A A, Bochkarev S G and Bychenkov V Y 2005 Ion acceleration in short-laser-pulse interaction with solid foils *Plasma Phys. Control. Fusion* **47** B869–77

[29] King M *et al* 2016 Ion acceleration and plasma jet formation in ultra-thin foils undergoing expansion and relativistic transparency *Nucl. Instrum. Methods Phys. Res.* **829** 02

[30] Powell H *et al* 2015 Proton acceleration enhanced by a plasma jet in expanding foils undergoing relativistic transparency *New J. Phys.* **17** 103033

[31] Huebl A *et al* 2020 Spectral control via multi-species effects in PW-class laser-ion acceleration *Plasma Phys. Control. Fusion* **62** 124003

[32] Robinson A P L, Bell A R and Kingham R J 2006 Effect of target composition on proton energy spectra in ultraintense laser-solid interactions *Phys. Rev. Lett.* **96** 035005